Compressible boundary layers over isotropic porous surfaces

Ludovico Fossà [*,†] and Pierre Ricco
School of Mechanical, Aerospace and Civil Engineering, Mappin Building, University of Sheffield, S13JD Sheffield, United Kingdom

(Received 11 June 2025; accepted 11 August 2025; published 29 September 2025)

A compressible laminar boundary layer developing over an isotropic porous substrate is investigated by asymptotic and numerical methods. The substrate is modeled as an array of cubes. The momentum and enthalpy balance equations are derived by volume averaging. The self-similar solution proposed by Tsiberkin [Transp. Porous Media **121**, 109 (2018)] for streamwise-growing permeability is extended to include compressibility, heat conduction, and a nonlinear drag. The velocity profile shows an inflection point at the free fluid-porous interfacial layer, below which it decreases to zero. A marked reduction of the adiabatic recovery temperature of the fluid and the velocity gradient at the interface is observed for high porosity, large grains, and relatively high Mach numbers. The temperature imposed at the bottom of the porous substrate has a negligible influence on the shear stresses.

DOI: 10.1103/5j49-bxxs

I. INTRODUCTION

Fluid flows over saturated porous media are common in industrial and engineering contexts [1–5]. Several theoretical, numerical and experimental studies have focused on the coupling between a free fluid and an adjacent saturated porous medium in confined geometries [6–8] and on wall-bounded flows through a semi-infinite porous medium [9–11]. Much less attention has been devoted to the coupling between an unbounded fluid and a porous medium. In Ref. [2], the authors studied the effects of a porous substrate on the heat transfer and the drag exerted by an overflowing fluid subject to a streamwise pressure gradient. They solved the steady, two-dimensional Navier-Stokes equations with a Darcy term and a Forchheimer term. The boundary-layer approximation was not imposed and the governing equations were elliptic, yet their results featured a marked parabolic character. Reference [3] modeled the influence of a uniform porous substrate on an incompressible Blasius boundary layer by expanding the streamfunction in a power series of $(K^*/x^*)^{1/2}$, where x^* is the streamwise coordinate and K^* is a sufficiently small permeability. They implicitly assumed continuity in the velocity and shear stresses across the fluid-porous interface [12]. Using a similar approach, Ref. [4] proposed a theoretical model for an incompressible laminar boundary layer over a porous flat plate and adopted the interfacial conditions of [13]. The pores were assumed to be small enough for the non-Darcian effects to be negligible below the interface.

*Contact author: ludovico-fossa@oist.jp
†Present address: Complex Fluids and Flows Unit, Okinawa Institute of Science and Technology Graduate University, 1919-1 Tancha, Onna-son, Kunigami-gun, Okinawa-ken 904-0495, Japan.

Theoretical and numerical analyses of compressible flows within porous media have drawn much less attention. Reference [14] used the volume-averaging approach [15,16] to study the effect of choking and included the Darcy, Forchheimer, and inertial terms in the analysis. The different roles of the advection and Forchheimer terms in compressible flows were also discussed in [17]. Porous substrates have been used to delay boundary-layer transition to turbulence in supersonic wind tunnels [18–20]. However, most studies have focused on the attenuation of small-amplitude acoustic disturbances in flat-plate boundary layers rather than the modification of the velocity profiles of the laminar base flows [19].

The modeling and computation of boundary-layer flows over and within porous surfaces of constant thickness and uniform permeability pose significant challenges, primarily because the thickness of the boundary layer grows downstream. Self-similar solutions cannot be derived when uniform porous substrates are considered [2,11]. The streamwise-marching computations have relied on the existence of a self-similar solution upstream [21,22].

A similarity solution was found in [5,23,24] for the case of an incompressible boundary layer on a porous substrate of infinite thickness and streamwise-increasing permeability. That analysis did not take the nonlinear Forchheimer term into account. It was concluded that neither the Brinkman nor the advection term can be neglected without losing important features of the momentum transfer and interfacial stability. Albeit stemming from an idealized setting, self-similar and local-similarity solutions permit us to overcome all these issues and to unravel physical mechanisms that are relevant to more realistic scenarios, particularly when the effects of compressibility are important [25,26]. The central aim of the present work is to extend Tsiberkin's solution to high-speed boundary layers. For the first time, the governing equations are derived by volume averaging, and the effects of nonlinear drag, compressibility, and heat conduction are found numerically.

II. MATHEMETICAL FRAMEWORK

The focus is on a two-dimensional, steady air flow over the top flat surface of an isotropic and uniform porous substrate. The substrate lies above a solid impermeable surface and is saturated with air. The governing equations for the fluid phase are derived by volume averaging the compressible Navier-Stokes equations [15,16,27–29]. The averaged *macroscopic* fluid quantities result from an upscaling process as the *microscopic* quantities are smoothed by applying a spatial filter $\overline{m}^*$ over a representative elementary volume (REV) that encloses portions of the fluid domain and the solid matrix. All dimensional quantities are denoted by the superscript $*$. When the top-hat filter $\overline{m}^* = 1/\Omega_0^*\,[\mathrm{m}^{-3}]$ [30,31] is used (where Ω_0^* is the total volume of the REV), the intrinsic volume average of the fluid phase within the REV is $\langle\cdot\rangle_f = 1/\Omega_0^* \int_{\Omega_0^*}[\cdot]\mathrm{d}\Omega^*$. The ratio of the fluid volume to the total volume of the REV defines the volume porosity $\theta_f = \Omega_f^*/\Omega_0^*$. The surface porosity is the ratio $\theta_{\partial ff} = (\partial\Omega_f)^*/(\partial\Omega_0)^*$, where $(\partial\Omega_f)^*$ is the portion of the external surface of the REV wetted by the fluid phase, and $(\partial\Omega_0)^*$ is the total external surface of the REV. A porous substrate with the ordered microstructure is considered (refer to Fig. 1). A cellular filter, which results from the double convolution of the top-hat filter, is employed [6,30,31]. The averaged macroscopic quantities are defined at the centroid of the REV and vary continuously across an interface of finite thickness at the top boundary of the substrate. To simplify the notation, the normalized filter $m = \overline{m}^*\Omega_0^*$ and the ratio $\Sigma_{fs}^* = (\partial\Omega_{fs})^*/\Omega_0^*\,(\mathrm{m}^{-1})$ are introduced, where $(\partial\Omega_{fs})^*$ is the fluid-solid interface surface within the REV [28]. The averaging operators read

$$\langle[\cdot]\rangle_f = \frac{1}{\Omega_0^*}\int_{\Omega_0^*} m[\cdot]\,\mathrm{d}\Omega^*, \tag{1a}$$

$$\langle[\cdot]n_j\rangle_{\partial fs}\Sigma_{fs}^* = \frac{1}{\Omega_0^*}\int_{(\partial\Omega_{fs})^*} m\,[\cdot]n_j\,\mathrm{d}(\partial\Omega^*), \tag{1b}$$

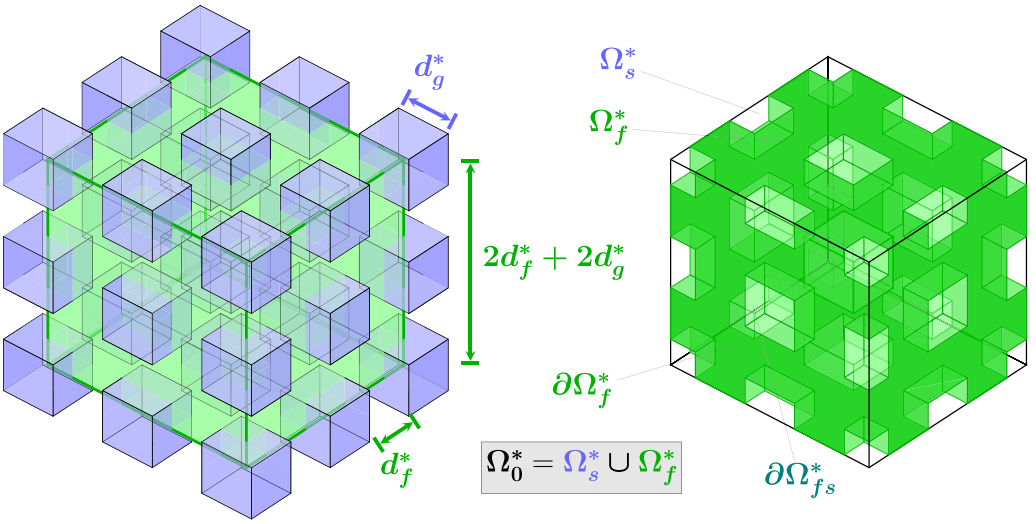

FIG. 1. Schematic of the microscopic structure of the porous substrate. On the left side, a cubic REV (green) of volume $\Omega_0^* = 8(d_g^* + d_f^*)^3$ is placed within an array of uniformly spaced solid grains (blue cubes) of size d_g^* and intergrain distance d_f^*. On the right, the volume of fluid enclosed by the REV is shown (green). The fluid and solid volume fractions, Ω_f^* and Ω_s^*, are also drawn along with the fluid-solid interface surface $(\partial\Omega_{fs})^*$ and the portion of the external surface of the REV occupied by the fluid $(\partial\Omega_f)^*$.

and the quantities are decomposed as the sum of their volume-averaged and fluctuating parts, $[\cdot] = \langle[\cdot]\rangle_f + \widetilde{[\cdot]}$, with $\langle\widetilde{[\cdot]}\rangle_f = 0$ [32]. The flow is described in a Cartesian frame of reference, where x^* and y^* define the streamwise and wall-normal coordinates, respectively. The intrinsic average of the gradient (or the divergence) of a tensor G_{ijk}^* of dimension 3 or lower (see Ref. [15], Eq. 2.3.29) takes the form

$$\theta_f \left\langle \frac{\partial G_{ijk}^*}{\partial x_\sigma^*} \right\rangle_f = \frac{\partial}{\partial x_\sigma^*}(\theta_f \langle G_{ijk}^* \rangle_f) + \int_{\partial\Omega_{fs}} \overline{m}^* \, G_{ijk}^* n_\sigma \mathrm{d}(\partial\Omega^*), \tag{2}$$

where n_i are the versors normal to the fluid-solid interface, and $\sigma = i$ for the gradient ($\sigma = j$ for the divergence). The pressure p^*, the density ρ^*, the temperature T^*, and the velocity components u_i^* are also introduced. Provided that $\partial^2 p^*/\partial x_j^{*2} = 0$ within the REV, the average of the pressure gradient can be expanded as (see Ref. [15], Eq. 2.3.48)

$$\theta_f \left\langle \frac{\partial p^*}{\partial x_i^*} \right\rangle_f = \theta_f \mathcal{T}_{ij} \frac{\partial \langle p \rangle_f^*}{\partial x_j^*} + \int_{\partial\Omega_{fs}} \overline{m}^* \, \widetilde{x}_i^* \frac{\partial \widetilde{p}^*}{\partial x_j^*} n_j \mathrm{d}(\partial\Omega^*), \tag{3}$$

where $\mathcal{T}_{ij}$ is the nondimensional tortuosity tensor, which is $(\theta_{\partial ff}/\theta_f)\delta_{ij}$ in an isotropic medium [15,28].

A. Governing equations

We consider the steady, two-dimensional form of the equations for mass conservation and balance for the streamwise and wall-normal momentum and the enthalpy. The solid matrix is assumed to be rigid. The divergence operator (2) is applied to the steady, two-dimensional mass conservation equation. By neglecting the mechanical-dispersion terms $\langle\widetilde{\rho}^*\widetilde{u}^*\rangle_f$ and assuming zero-mass transport across the impermeable fluid-solid interfaces within the REV, one finds [15]

$$\frac{\partial}{\partial x_j^*}(\theta_f \langle \rho^* \rangle_f \langle u_j^* \rangle_f) = 0, \tag{4}$$

where the volume porosity is, in general, a smooth function of x^* and y^*. The momentum balance takes the form

$$\theta_f \langle \rho^* \rangle_f \langle u_j^* \rangle_f \frac{\partial \langle u_i^* \rangle_f}{\partial x_j^*} + \theta_f \mathcal{T}_{ij} \frac{\partial \langle p^* \rangle_f}{\partial x_j^*} = \theta_f \left\langle \frac{\partial \tau_{ij}^*}{\partial x_j^*} \right\rangle_f - \left\langle \widetilde{x}_i^* \frac{\partial \widetilde{p}^*}{\partial x_j^*} n_j \right\rangle_{\partial fs} \Sigma_{fs}^*. \tag{5}$$

The solid and fluid phase velocities are zero at the solid-fluid interface, and the divergence of the shear stresses τ_{ij}^* expands as (see Ref. [15], Eq. 2.6.32)

$$\begin{aligned} \theta_f \left\langle \frac{\partial \tau_{ij}^*}{\partial x_j^*} \right\rangle_f = {} & \frac{\partial}{\partial x_j^*} \left[\langle \mu^* \rangle_f \left(\frac{\partial (\theta_f \langle u_i^* \rangle_f)}{\partial x_j^*} + \frac{\partial (\theta_f \langle u_j^* \rangle_f)}{\partial x_i^*} \right) \right] + \frac{\partial}{\partial x_i^*} \left[\langle \lambda^* \rangle_f \frac{\partial (\theta_f \langle u_k^* \rangle_f)}{\partial x_k^*} \right] \\ & + \left\langle \mu^* \left(\frac{\partial u_i^*}{\partial x_j^*} + \frac{\partial u_j^*}{\partial x_i^*} \right) \right\rangle_{\partial fs} \Sigma_{fs}^* - \frac{\langle \lambda^* \rangle_f}{\theta_f} \frac{\partial (\theta_f \langle u_k^* \rangle_f)}{\partial x_k^*} \frac{\partial \theta_f}{\partial x_i^*}, \end{aligned} \tag{6}$$

where λ^* is the second coefficient of viscosity, and the last term is obtained by employing the identity $\partial \theta_f / \partial x_i^* = \langle -n_i \rangle_{\partial fs} \Sigma_{fs}^*$. The surface integrals on the right-hand side of Eqs. (5) and (6) are often modeled using a permeability tensor [28,33] and a Forchheimer tensor [34]. The latter is a nonlinear correction to Darcy's law which arises at large microscopic Reynolds numbers [31,34]. While the departure from the linear Darcian regime is very well known and has been widely reported in numerical and laboratory experiments, the mathematical modeling and the physical nature of the Forchheimer correction are a matter of current research. Nonlinear corrections with a cubic, quadratic, and power-law dependence on the velocity have been reported for different ranges of the microscopic Reynolds numbers on pretransitional fluid flows inside porous media [35,36]. The surface integral is modeled as the sum of a linear and a quadratic drag [6,34,37],

$$\begin{aligned} & \left\langle -\widetilde{x}_i^* \frac{\partial \widetilde{p}^*}{\partial x_j^*} n_j + \mu^* \left(\frac{\partial u_i^*}{\partial x_j^*} + \frac{\partial u_j^*}{\partial x_i^*} \right) n_j \right\rangle_{\partial fs} \Sigma_{fs}^* \\ & \quad = -\langle \mu^* \rangle_f \theta_f^2 (K^{*-1})^{ij} \langle u_j^* \rangle_f - \langle \rho^* \rangle_f \theta_f^2 [(K^{*-1})^{ik} (c_{F,kjl}^* \langle u_l^* \rangle_f)] \langle u_j^* \rangle_f, \end{aligned} \tag{7}$$

where the inverse of the permeability tensor K_{ij}^* and the Forchheimer tensor $c_{F,kjl}^*$ have been introduced. The coefficients of the Darcy and Forchheimer terms are often modeled using the Kozeny-Carman and Ergun relations [6,34], that is,

$$K_{ij}^* = \frac{\theta_f^3}{(1-\theta_f)^2} \frac{d_g^{*2}}{A} \delta_{ij} \quad \text{and} \quad c_{F,ijk}^* = \frac{\theta_f}{1-\theta_f} \frac{d_g^*}{B} \delta_{ijk}, \tag{8}$$

where the grain size $d_g^* = d_g^*(x^*, y^*, d_{g0}^*)$ is assumed to be a smooth function of x^*, y^* and the reference value d_{g0}^*. A and B are empirical coefficients [34]. Similar forms of the Kozeny-Carman relation of the type $K^* = C^* \theta_f^m / (1-\theta_f)^n$, where C^* is a dimensional parameter and m and n are positive real constants, have also been used [38]. The Forchheimer coefficient $c_{F,ijk}^*$ is sometimes modeled as an exponential function of K^* [39,40]. Although the closure model (7) may no longer hold in the compressible regime, where the seepage velocity can be as large as $10^2\ \mathrm{ms}^{-1}$ for high porosity [18], Eqs. (7) and (8) are used with the incompressible values $A = 180$ and $B = 100$ because of the lack of experimental data. Some authors [34,41,42] have argued that the inertial terms should be removed from the equations when a quadratic Forchheimer correction is included, while others [6,13,43] have pointed out that they are not negligible at the free fluid-porous interface or in compressible porous media flows [14,44,45]. The coexistence of the inertial terms and the Forchheimer terms in the momentum equation is still a matter of debate. We shall retain both terms and adopt the volume-averaging framework of [31].

Applying the operators (2) to the static enthalpy balance yields

$$\theta_f \langle \rho^* \rangle_f \langle u_j^* \rangle_f \frac{\partial \langle T^* \rangle_f}{\partial x_j^*} = \frac{\langle \mu^* \rangle_f}{\theta_f} \left[\frac{\partial (\theta_f \langle u_i^* \rangle_f)}{\partial x_j^*} \right]^2 + \frac{\langle \lambda^* \rangle_f}{\theta_f} \left[\frac{\partial (\theta_f \langle u_k^* \rangle_f)}{\partial x_k^*} \right]^2 + \frac{\langle \mu^* \rangle_f}{\theta_f} \frac{\partial (\theta_f \langle u_i^* \rangle_f)}{\partial x_j^*} \frac{\partial (\theta_f \langle u_j^* \rangle_f)}{\partial x_i^*} + \frac{\partial}{\partial x_j^*} \left(\theta_f \langle k^* \rangle_f \mathcal{T}_{jk} \frac{\partial \langle T^* \rangle_f}{\partial x_k^*} \right), \quad (9)$$

where k^* is the thermal conductivity. The perfect gas equation becomes $\langle p^* \rangle_f = \langle \rho^* \rangle_f \mathcal{R}^* \langle T^* \rangle_f$, where $\mathcal{R}^* = 287.05\,\mathrm{J\,kg^{-1}\,K^{-1}}$ is the specific gas constant of air. We shall assume that the microscopic temperature gradients of the fluid phase at the surface of the solid grains are negligible and that the fluid and solid phases are in local thermal equilibrium (LTE) $\langle T^* \rangle_f = \langle T^* \rangle_s$ (see Ref. [15], Eq. 2.6.121). It is important to note that although the LTE hypothesis has been invoked in the context of steady porous media flows with moderate θ_f [3], it is not valid in general. Reference [46] computed the evolution of the temperature profiles of the fluid and solid phases over a flat plate immersed in a uniform porous medium and showed that the LTE assumption is not valid near the leading edge. Thermal equilibrium is only achieved at moderate downstream locations when the conductivity of the fluid phase is much larger than that of the solid phase, $k_f^*/k_s^* \gg 1$, or when the volume porosity is very high, $\theta_f \to 1$. A similar flow configuration was investigated in [47] for the case of an iron-made, regular-microstructure solid matrix ($k_s^* = 52\,\mathrm{W m^{-1}\,K^{-1}}$) saturated with water and air. The temperature profiles for the fluid and solid phases differed significantly at short downstream distances $x^*/d_{g0}^* = O(1)$. One must exercise caution when invoking the LTE hypothesis as local nonequilibrium may occur, especially in the vicinity of the leading edge.

We shall assume the LTE hypothesis to be valid in the porous layer because we expect the velocity to be very small (and the static temperature to be comparable to the adiabatic recovery temperature) below the porous-fluid interface. The static enthalpy balance of the fluid phase and the internal energy balance of the solid phase then reduce to the thermal conduction and thermal convection terms [46]. When an adiabatic condition is imposed underneath, the temperature across the substrate is almost uniform and the interphasial heat exchange is negligible.

The fluid flow is uniform away from the substrate because the streamwise pressure gradient is null. A thin boundary layer forms above the fluid-porous interface. The velocity components, the density, the temperature, and the transport coefficients are normalized by their free-stream values, denoted by the subscript ∞. The macroscopic pressure $\langle p^* \rangle_f$ is scaled by $\rho_\infty^* U_\infty^{*2}$, where U_∞^* is the free-stream velocity. The free-stream Reynolds number is $\mathrm{Re} = \rho_\infty^* U_\infty^* L^*/\mu_\infty^* \gg 1$, where μ_∞^* is the free-stream dynamic viscosity and L^* is a characteristic large streamwise length. The Darcy number, based on the characteristic grain size d_{g0}^*, is $\mathrm{Da} = d_{g0}^{*2}/L^{*2} \ll 1$ and the free-stream Mach number is $\mathrm{Ma} = U_\infty^*/c_\infty^* = O(1)$, where $c_\infty^* = (\gamma \mathcal{R}^* T_\infty^*)^{1/2}$ is the speed of sound in the free stream, and $\gamma = 1.4$ is the heat capacity ratio. The dynamic viscosity is modeled using Sutherland's law,

$$\frac{\mu^*}{\mu_\infty^*} = \left(\frac{T^*}{T_\infty^*} \right)^{3/2} \frac{\chi^* + T_\infty^*}{\chi^* + T^*}, \quad (10)$$

where $\chi^* = 110\,\mathrm{K}$ is the Sutherland temperature. The parabolic character of the solution obtained by [2] resulted from the concurrent contribution of the Brinkman, Forchheimer, and advective terms, all of which need to be retained while performing a rigorous asymptotic analysis. The Forchheimer term cannot satisfy the boundary-layer approximation when scaled by a factor $\rho_\infty^* U_\infty^*/d_{g0}^* \gg 1$ [24]. The Darcy and Forchheimer terms are a parametrization of the surface integrals in (7), and appropriate scaling must be applied to the integrating functions themselves. The characteristic length of the REV Σ_{fs}^{*-1} scales as d_g^*, the velocity scales as U_∞^* [8,37], and the microscopic pressure fluctuations $\widetilde{p}^*$ scale as $\mu_\infty^* U_\infty^*/d_g^*$ [34].

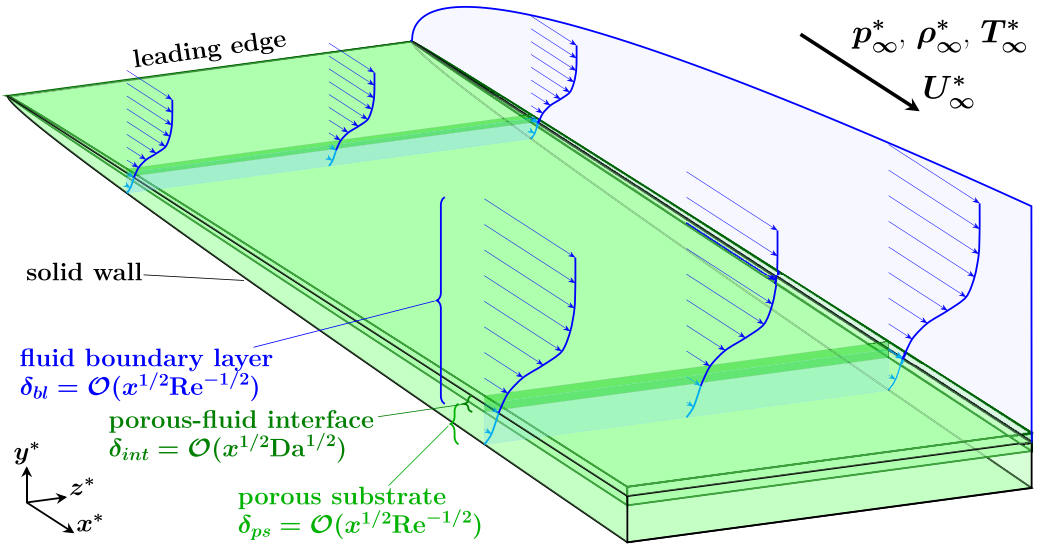

FIG. 2. Schematic of the self-similar flow. A boundary layer of thickness δ_{bl} (blue) evolves over an isotropic porous substrate of streamwise-increasing thickness δ_{ps} (green). The figure is not to scale.

B. Porous-free fluid interface

A schematic of the self-similar, coupled porous substrate-boundary layer flow is shown in Fig. 2. As in classic boundary-layer theory [25], the flow properties are expected to vary in a region of thickness $O(\mathrm{Re}^{-1/2})$ near the top surface of the substrate. Hereafter, the averaging operators $\langle\cdot\rangle_f$ are omitted for clarity, with no risk of ambiguity regarding volume averaging. The limiting form of Eqs. (4), (5), and (9) for $\mathrm{Re} \gg 1$ and $\mathrm{Da} \ll 1$ is parabolic in x and reads [48]

$$\frac{\partial}{\partial x}\left(\frac{\theta_f u}{T}\right) + \frac{\partial}{\partial y}\left(\frac{\theta_f v}{T}\right) = 0, \tag{11a}$$

$$\frac{\theta_f u}{T}\frac{\partial u}{\partial x} + \frac{\theta_f v}{T}\frac{\partial u}{\partial y} = \frac{\partial}{\partial y}\left[\mu\frac{\partial(\theta_f u)}{\partial y}\right] - \frac{\theta_f^2}{\widehat{\kappa}_p^2}\left(\frac{\mu u}{K} + \frac{\theta_f \widehat{c}_F}{K^{1/2}}\frac{u^2}{T}\right), \tag{11b}$$

$$\frac{\theta_f u}{T}\frac{\partial T}{\partial x} + \frac{\theta_f v}{T}\frac{\partial T}{\partial y} = \frac{\mu}{\theta_f}\left[\frac{\partial(\theta_f u)}{\partial y}\right]^2 + \frac{\partial}{\partial y}\left(\theta_{\partial ff}\frac{\mu}{Pr}\frac{\partial T}{\partial y}\right), \tag{11c}$$

where the streamwise pressure gradient is absent and the perfect gas equation is $\rho T = 1$. A self-similar solution cannot be retrieved in the general case where the Forchheimer coefficient is a function of a streamwise-varying grain diameter $d_g^* = d_{g0}^*(2x)^{1/2}$. It can only be obtained if the permeability K^* is a function of the streamwise-varying grain diameter $d_g^* = d_{g0}^*(2x)^{1/2}$ and the Forchheimer coefficient $\widehat{c}_F$ is a function of a constant grain diameter $d_g^* = d_{g0}^*$. d_{g0}^*, i.e., $\widehat{c}_F = \widehat{c}_F(\theta_f, d_{g0}^*)$. When the low-speed, incompressible closure model (7) is considered, this choice is equivalent to a local-similarity assumption. Here $K = \theta_f^3/[(1-\theta_f)^2 A] = O(1)$, $\widehat{c}_F = A^{1/2}\mathrm{ReDa}/(B\mathrm{Da}^{1/2}\theta_f^{3/2}) = O(1)$, $\widehat{\kappa}_p^2 = \mathrm{ReDa}(d_g^*/d_{g0}^*)^2 = O(1)$ [5], $A = O(1)$, and $B = O(\mathrm{Da}^{-1/2})$. The Prandtl number of air is $\mathrm{Pr} = c_p^*\mu_\infty^*/k_\infty^* = 0.71$ and $k(T) = \mu(T)$ [25]. A detailed derivation of the self-similar momentum equation and the Darcy-Forchheimer term is found in Appendix A.

A no-slip, no-penetration condition is imposed at the bottom solid wall of the substrate. The

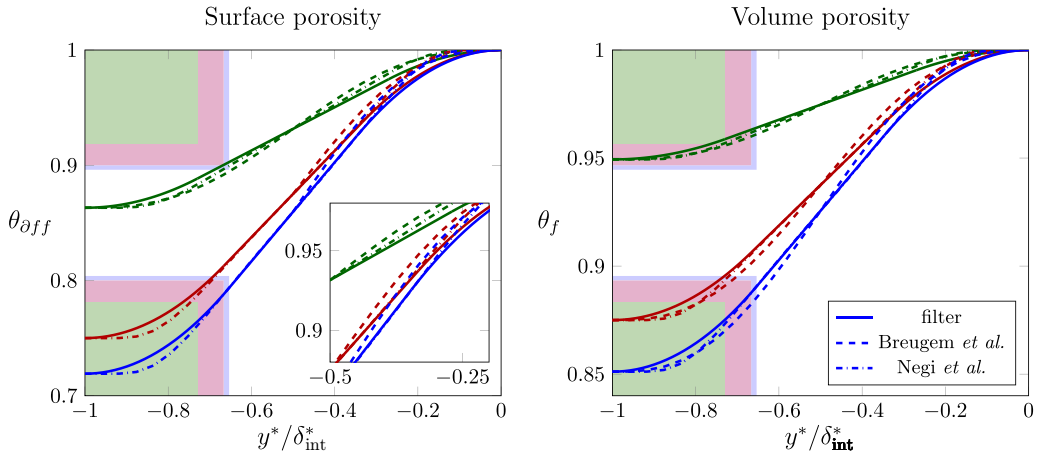

FIG. 3. Distribution of the volume and surface porosity across the interface. Comparison of the model equations of [31] (dashed curves) and [49] (dash dot curves) (14) with the results obtained by computing the convolution integral of the cellular filter across the porous-free fluid interfacial layer of thickness $\delta^*_{\rm int}$ (13) (solid curves) for $Q = 0.37$ (green), $Q = 0.5$ (red), and $Q = 0.53$ (blue). Green, red, and blue solid grains of size $d^*_g = \delta^*_{\rm int} Q/(1+Q)$ are drawn at the bottom side of the interface for comparison.

boundary conditions read

$$u(x, y_w) = 0, \quad u(x, \infty) = 1,$$
$$\frac{\partial T}{\partial y}(x, y_w) = 0, \quad T(x, \infty) = 1, \tag{12}$$

where the subscript w denotes the bottom solid wall. The top surface of the porous substrate is flat and located at a height $y^*_{\rm int}$. The thickness of the interface is $\delta_{\rm int} = O(\mathrm{Da}^{1/2})$ [50] and is therefore comparable to that of the boundary layer because $\delta_{\rm int}/\delta_{\rm bl} = O(\mathrm{Re}^{1/2}\mathrm{Da}^{1/2}) = O(1)$. The volume and surface porosity vary smoothly across the interface. Their uniform values below the interface are $\theta_{fp} = 1 - Q^3$ and $(\theta_{\partial ff})_p = 1 - Q^2$, respectively, where $Q = d^*_g/(d^*_f + d^*_g)$. Here, $d^*_f = d^*_f(x^*, y^*, d^*_{f0})$, where d^*_{f0} is a characteristic constant. The interfacial thickness is $\delta^*_{\rm int} = d^*_g(1+Q)/Q$. The distribution of θ_f and $\theta_{\partial ff}$ is obtained analytically by sweeping the averaging operator (1) across the interfacial region [51]. Repeating this procedure for arbitrary d^*_g and d^*_f yields the analytical piecewise-polynomial curve shown in Fig. 3 (solid curves),

$$\theta_{\partial ff}\left(\frac{y^*}{\delta^*_{\rm int}}\right) = 1 \quad \text{for} \quad \frac{y^*}{\delta^*_{\rm int}} \geqslant 0, \tag{13a}$$

$$\theta_{\partial ff}\left(\frac{y^*}{\delta^*_{\rm int}}\right) = 1 - \frac{Q}{(d^*_f + d^*_g)^2}\int_{-d^*_g - d^*_f}^{-d^*_g - d^*_f - y^*} (d^*_g + d^*_f + \check{y}^*)\mathrm{d}\check{y}^*$$
$$= 1 - \frac{Q}{2}(1+Q)^2\left(\frac{y^*}{\delta^*_{\rm int}}\right)^2 \quad \text{for} \quad -\frac{Q}{1+Q} \leqslant \frac{y^*}{\delta^*_{\rm int}} < 0, \tag{13b}$$

$$\theta_{\partial ff}\left(\frac{y^*}{\delta^*_{\rm int}}\right) = 1 - \frac{Q}{(d^*_f + d^*_g)^2}\int_{-d^*_f - 2d^*_g - y^*}^{-d^*_g - d^*_f - y^*} (d^*_g + d^*_f + \check{y}^*)\mathrm{d}\check{y}^*$$
$$= 1 + Q^3\left[\frac{1}{2} + \frac{1+Q}{Q}\frac{y^*}{\delta^*_{\rm int}}\right] \quad \text{for} \quad -\frac{1}{1+Q} \leqslant \frac{y^*}{\delta^*_{\rm int}} < -\frac{Q}{1+Q}, \tag{13c}$$

$$\theta_{\partial ff}\left(\frac{y^*}{\delta^*_{\rm int}}\right) = 1 - \frac{Q}{(d^*_f + d^*_g)^2}\left[\int_{-d^*_g - d^*_f}^{-2d^*_g - 2d^*_f - y^*} (d^*_g + d^*_f + \check{y}^*)\mathrm{d}\check{y}^* + \int_{0}^{-d^*_f - 2d^*_g - y^*} (d^*_g + d^*_f + \check{y}^*)\mathrm{d}\check{y}^* + \int_{-d^*_g - d^*_f - y^*}^{0} (d^*_f + d^*_g - \check{y}^*)\mathrm{d}\check{y}^*\right]$$

$$= 1 + Q\left[\frac{(1+Q^2)}{2} + (1+Q)^2\frac{y^*}{\delta^*_{\rm int}} + \frac{(1+Q)^2}{2}\left(\frac{y^*}{\delta^*_{\rm int}}\right)^2\right] \quad \text{for} \quad -1 \leqslant \frac{y^*}{\delta^*_{\rm int}} < -\frac{1}{1+Q}, \tag{13d}$$

$$\theta_{\partial ff}\left(\frac{y^*}{\delta^*_{\rm int}}\right) = 1 - Q^2 \quad \text{for} \quad \frac{y^*}{\delta^*_{\rm int}} < -1. \tag{13e}$$

Reference [31] approximated (13) with a fifth-order polynomial. Instead, an interpolating exponential function is used in this work [49],

$$\frac{\theta_f(\widetilde{y}) - \theta_{fp}}{1 - \theta_{fp}} = \frac{\theta_{\partial ff}(\widetilde{y}) - (\theta_{\partial ff})_p}{1 - (\theta_{\partial ff})_p} = \left[1 + \exp\left(\frac{C}{\widetilde{y}} + \frac{C}{\widetilde{y}+1}\right)\right]^{-1}, \tag{14}$$

where $\widetilde{y} = (y^* - y^*_{\rm int})/\delta^*_{\rm int}$, $C = 0.75$. As shown in Fig. 3, the agreement between the analytical piecewise curve and the exponential model (14) is excellent.

C. Self-similar solution

A similarity solution of the differential system (11) is sought in this section. First, the Dorodnitsyn-Howarth variable [25]

$$\overline{y} = \int_0^y \rho(x, \check{y})\mathrm{d}\check{y} \tag{15}$$

is introduced. A streamfunction $\psi(x, \overline{y})$ is defined so that the continuity equation (11a) is satisfied,

$$u = \frac{1}{\theta_f}\frac{\partial \psi}{\partial \overline{y}}, \quad v = -\frac{T}{\theta_f}\frac{\partial \psi}{\partial x}. \tag{16}$$

Following a standard procedure in the derivation of the self-similar boundary layer equations, a decomposition of ψ and $\overline{y}$ is sought in the form

$$\psi(x, \overline{y}) = (\alpha x)^a F(x, \eta), \quad \overline{y} = (\alpha x)^b \eta, \tag{17}$$

where α, a, and b are real constants. Inspection of (12) shows that T cannot be a function of x in homoenthalpic flows and that no similarity solution is possible if an inhomogeneous Neumann condition for the temperature is imposed at the solid wall underneath the substrate. Since the top of the substrate is flat, the wall-normal porosity distribution (14) is a function of η alone when both $\delta_{\rm int}$ and δ_{ps} are $O(x^b)$. Following [5,23,24], the grain size and the intergrain distance are assumed to be smooth functions of x, $d^*_g = d^*_{g0}(\alpha x)^{c/2}$ and $\widehat{\kappa}_p = \kappa_p(\alpha x)^c$, where

$$\kappa_p^2 = \mathrm{ReDa} = \frac{\rho^*_\infty U^*_\infty d^{*2}_{g0}}{\mu^*_\infty L^*} = O(1) \tag{18}$$

is the control parameter defined by [23]. The parameter distills the effect of the linear Darcy drag for given free-stream conditions and grain size. A similarity solution exists for $a = b = 1/2$, $c = 1$, and $\alpha = 2$. Equations (11b) and (11c) then reduce to a system of coupled ordinary differential equations

$$\left(\frac{\mu}{T}F''\right)' + F\left(\frac{F'}{\theta_f}\right)' - C_D\mu T\frac{(1-\theta_f)^2}{\theta_f^2}F' - C_F\frac{1-\theta_f}{\theta_f^2}(F')^2 = 0, \tag{19a}$$

$$\frac{1}{\mathrm{Pr}}\left(\theta_{\partial ff}\frac{\mu T'}{T}\right)' + FT' + \frac{(\gamma-1)}{\theta_f}\frac{\mu}{T}\mathrm{Ma}^2(F'')^2 = 0, \tag{19b}$$

where the primes denote differentiation with respect to the similarity variable

$$\eta = \frac{\overline{y}}{(2x)^{1/2}}, \tag{20}$$

and the coefficients of the Darcy and the Forchheimer terms are $C_D = A/\kappa_p^2$ and $C_F = A/(BDa^{1/2}) = O(1)$, respectively. Equations (19) are subject to the boundary conditions $F = F' = T' = 0$ at the bottom solid wall ($\eta = 0$) and $F', T \to 1$ as the free stream is approached ($\eta \to \infty$). For the first time, a self-similar form of the governing equations has been derived for compressible flow over a porous substrate with streamwise-increasing permeability, using a closure model with a constant Forchheimer coefficient. Equations (19) reduce to the compressible Blasius solution [25] above the interface, where $\theta_f, \theta_{\partial ff} = 1$. The velocity components are

$$u(\eta) = \frac{F'}{\theta_f}, \tag{21a}$$

$$v(\eta) = \frac{1}{\theta_f(2x)^{1/2}}(-TF + \eta_c TF'), \tag{21b}$$

and $\eta_c = T^{-1}\int_0^\eta T(\check{\eta})\mathrm{d}\check{\eta}$. The nondimensional thickness of the fluid boundary layer, the fluid-porous interface, and the porous substrate are $\delta_{\mathrm{bl}} = O(x^{1/2}\mathrm{Re}^{-1/2})$, $\delta_{\mathrm{int}} = O(x^{1/2}\mathrm{Da}^{1/2})$, and $\delta_{ps} = O(x^{1/2}\mathrm{Re}^{-1/2})$, respectively. The thickness of the porous substrate can be written explicitly as a function of the distance from the leading edge, i.e., $\delta_{ps} = C_{ps}x^{1/2}\mathrm{Re}^{-1/2}$ or $\delta_{ps} = C_{ps}\kappa_p^{-1/2}x^{1/2}\mathrm{Da}^{1/2}$, where $C_{ps} = O(1)$ is a design parameter. The interfacial continuity of the surface-averaged tangential velocity $\theta_f u$ derived by [13] is recovered from (21a) for small κ_p ($\delta_{\mathrm{int}}/\delta_{\mathrm{bl}} \ll 1$).

The system (19) is solved by means of a second-order accurate block-elimination algorithm where nonlinearity is treated with the Newton-Raphson method [22]. A complete description of the numerical procedures is presented in Appendix B. A uniform grid was employed, and the computations were performed with $N = 4000$ and 20 000 points to ensure grid independency. The residuals were strictly kept below 10^{-12}. The interfacial thickness in the η-space,

$$(\Delta\eta)_{\mathrm{int}} = \frac{(\Delta y)_{\mathrm{int}}}{T_{\mathrm{av}}} = \frac{\kappa_p}{T_{\mathrm{av}}}\frac{1+Q}{Q}, \tag{22}$$

depends on the average temperature of the interfacial region T_{av} and is determined iteratively by solving the governing equations (19) for tentative Δy_{int} and $\Delta\eta_{\mathrm{int}}$ until the computed values of T_{av} satisfy (22). The values of $(\Delta y)_{\mathrm{int}}$, T_{av}, and $(\Delta_\eta)_{\mathrm{int}}$ are tabulated in Table III.

III. RESULTS

The results were obtained using physical parameters representative of real supersonic and hypersonic wind-tunnel conditions, as listed in Tables I and II. The corresponding numerical parameters, such as the factor Q, the interfacial thicknesses $(\Delta y)_{\mathrm{int}}$ and $(\Delta\eta)_{\mathrm{int}}$, and the surface temperature T_{av}, are provided in Table III for reference.

The flow is studied for different values of the free-stream Mach number, the static pressure and temperature, the reference grain size d_{g0}^*, and the volume porosity below the interface θ_{fp}. The

TABLE I. Wind tunnel measurements of compressible boundary layers over impermeable flat plates. Data are retrieved from [52] (GB02), [53] (M01), and [20] (R23).

Ref.	Ma	p_o^* (kPa)	T_o^* (K)	p_∞^* (kPa)	T_∞^* (K)	$T_w^*/T_{\mathrm{ad},w}^*$	δ_{99}^* (mm)[a]
GB02	2.98	31	290	0.87	104	1.1	[1.8, 3.3]
M01	5.92	1080	390	0.74	49	1	[1.8, 2.2]
R23	6.1	[490, 3044]	473	56.03	[54.25, 57.81]	n.a.	n.a.

[a]Measured between $x = 89$ mm and $x = 305$ mm (GB02) and at $x = 96$ mm (M01).

combination of these physical parameters determines κ_p, C_D, C_F, and $(\theta_{\partial ff})_p$. The values relevant to the investigated cases are listed in Table II. For every case, the letter (A, B, or C) defines a set of free-stream conditions, while the number (1 or 2) defines d_{g0}^*. The dimensional thickness of the Blasius boundary layer at $x^* = L^*$ is $\delta_{99}^* = \widehat{\delta}_{99}(\nu_\infty^* L^*/U_\infty^*)^{1/2}$. Here $\widehat{\delta}_{99} = \sqrt{2}\int_0^{\eta_{99}} T(\check{\eta})\mathrm{d}\check{\eta}$ increases with Ma and is a function of γ, Pr, and the temperature boundary condition at the bottom solid wall. The values of δ_{99}^*, estimated in Table II, are in good agreement with wind tunnel measurements (refer to Table I). The stagnation pressure is $p_\circ^*$, the stagnation temperature is $T_\circ^*$, the dimensional wall temperature is T_w^*, and the adiabatic recovery temperature of the Blasius solution is $T_{\mathrm{ad},w}^*$.

Results for an incompressible, isothermal ($T_{\mathrm{av}} = 1$) boundary layer at Ma $= 0.01$ (cases A1 and A2) are shown in Fig. 4. The first and second derivative of the streamfunction F are plotted as functions of η for two different values of the volume porosity θ_{fp} and characteristic grain size d_{g0}^* (κ_p). The top of the free fluid-porous interfacial region described in Fig. 3 is located at $\eta = \eta_{\mathrm{int}}$ (thin horizontal blue line in Fig. 4) and its lower boundary is denoted by a thin horizontal black or red line for each case (also refer to Figs. 5 and 6). The Blasius solution for a flat-plate boundary layer is also drawn (blue curve), its solid wall being located at the top of the interfacial region for comparison [31], where $\theta_f = 1$ and the Darcy and Forchheimer terms become zero. The slip velocity, obtained by evaluating (21a) at the interface, increases with θ_{fp} and d_{g0}^*, in qualitative agreement with the results of [23,24], which showed increasing interfacial velocity for increasing values of the control parameter κ_p^2 without the Forchheimer correction. The incompressible intrinsic shear stresses $\tau = (F'' - F'\theta_f'/\theta_f)/\theta_f$ [i.e., the shear stresses multiplied by $(2x)^{1/2}$; refer to Ref. [4],

TABLE II. Physical parameters. The volume and surface porosity in the region below the interface are denoted with θ_{fp} and $(\theta_{\partial ff})_p$, respectively.

Ma	p_∞^* (kPa)	$p_\circ^*$ (kPa)	T_∞^* (K)	$T_\circ^*$ (K)	U_∞^* (ms^{-1})	δ_{99}^* (mm)	d_{g0}^* (μm)	κ_p^2	case
0.01	100	100	293	293	3.43	3.3	100	0.02	A1
							200	0.09	A2
3	0.82	30.12	104	291	611	1.8	100	0.24	B1
							200	0.96	B2
6	0.76	1200	60	492	927	1.6	100	1.10	C1
							200	4.35	C2

Q	$1-Q$	$(\theta_{\partial ff})_p = 1-Q^2$	$\theta_{fp} = 1-Q^3$	$\delta_{\mathrm{int}}^*/d_g^* = (1+Q)/Q$
0.22	0.78	0.95	0.99	5.55
0.37	0.63	0.86	0.95	3.70
0.5	0.5	0.75	0.875	3
0.53	0.47	0.72	0.85	2.89

TABLE III. Numerical parameters used in the computations.

Ma	d^*_{g0} [μm]	κ_p^2	C_D	C_F	θ_{fp}	Q	$(\Delta y)_{\text{int}}$	T_{av}	$(\Delta\eta)_{\text{int}}$	case
0.01	100	0.02	9000	1800	0.85	0.53	0.43	1	0.43	A1
					0.95	0.37	0.57	1	0.57	
	200	0.09	2000	900	0.85	0.53	0.86	1	0.86	A2
					0.95	0.37	1.11	1	1.11	
3	100	0.24	750	1800	0.85	0.53	1.42	2.43	0.58	B1
					0.95	0.37	1.83	2.31	0.79	
	200	0.96	187.5	900	0.85	0.53	2.83	2.32	1.22	B2
					0.95	0.37	3.63	2.23	1.63	
6	100	1.10	163.6	1800	0.85	0.53	3.01	6.74	0.45	C1
					0.95	0.37	3.88	6.28	0.62	
	200	4.35	41.3	900	0.85	0.53	6.02	6.39	0.94	C2
					0.95	0.37	7.76	5.64	1.38	

Eqs. 116 and 117] are mostly influenced by F'' and grow to a peak located at the interface in all cases. Both F' and F'' undergo a rapid decay across the interface and within the porous region.

The results of the supersonic cases are shown in Figs. 5 and 6. Adiabatic boundary conditions were imposed at the solid wall below the substrate. The profiles for F' and F'' are shown along with the temperature T (bottom left) and the local Mach number $M = u^*/(\gamma \mathcal{R}^* T^*)^{1/2} = \text{Ma}\, F'/(\theta_f T^{1/2})$ (bottom right). The slip velocity increases and F'' decreases with increasing d^*_{g0} and θ_{fp} for constant free-stream conditions. Moreover, the temperature T does not recover the adiabatic value of the compressible Blasius solution and it reduces sharply at the interface when a porous substrate is introduced. The reduction becomes more marked with increasing κ_p and θ_{fp}. The peak of F'' is not sensitive to the geometry of the substrate. The influence of the porous substrate on the velocity profiles extends far from the interface, where F'' is reduced. As the F' profile shifts towards the interface and the magnitude of T decreases, the local Mach number M increases across the boundary layer (refer to the bottom right plots of Figs. 5 and 6). The insets in the bottom-right plot of Figs. 5 and 6 show that M is always well below unity near the bottom boundary of the

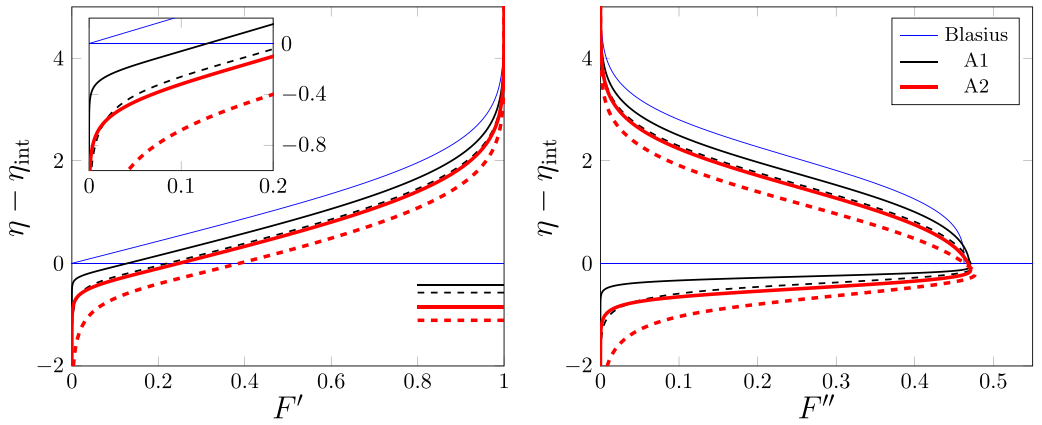

FIG. 4. First (left plot) and second (right plot) derivative of F as a function of η for an incompressible flow (Ma = 0.01). The black and red curves show cases A1 and A2, respectively, for $\theta_{fp} = 0.85$ (solid) and $\theta_{fp} = 0.95$ (dashed). The Blasius solution over a nonpermeable wall is plotted in blue for comparison. The top boundary of the interfacial region is located at η_{int} (blue line), while the bottom one is marked by the horizontal lines for each case.

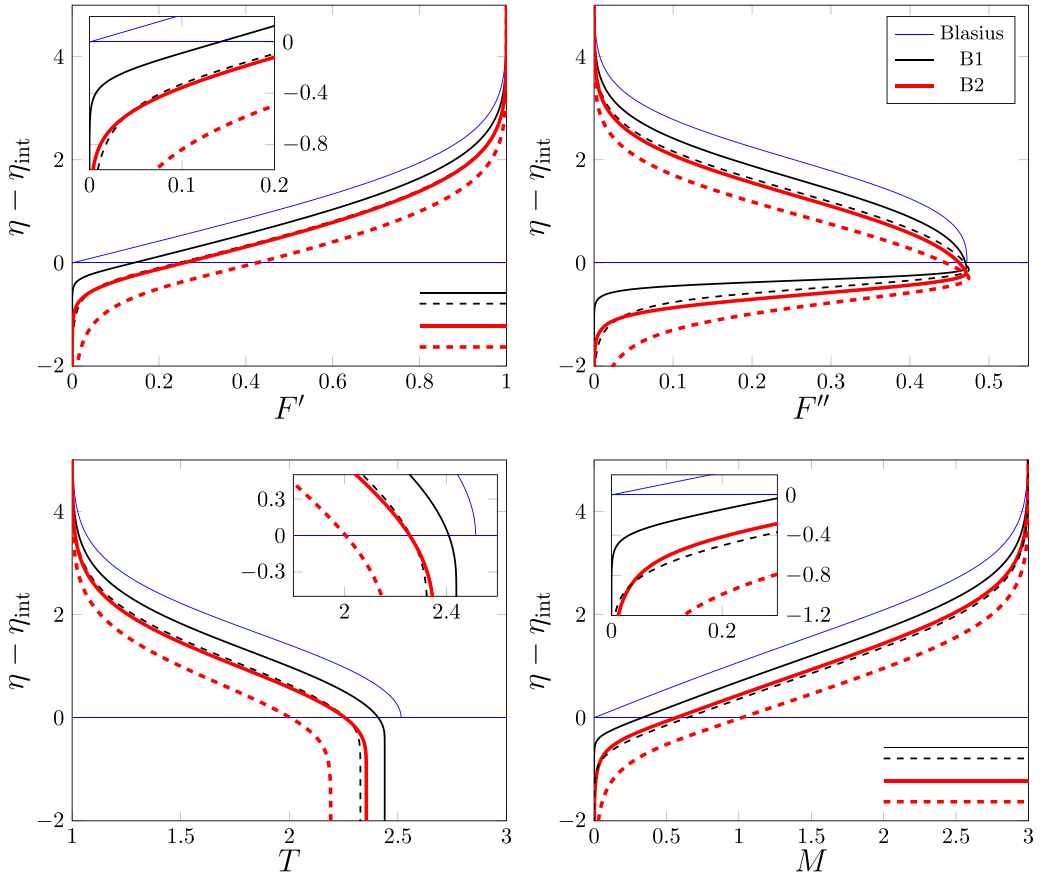

FIG. 5. First (top left) and second derivative (top right) of F as a function of η for a supersonic flow at $\mathrm{Ma} = 3$. The static temperature T and the local Mach number M are shown in the bottom-left and bottom-right plots, respectively. The black and red curves show cases B1 and B2, respectively, for $\theta_{fp} = 0.85$ (solid) and $\theta_{fp} = 0.95$ (dashed). The Blasius solution over a nonpermeable wall is plotted in blue for comparison. The top boundary of the interfacial region is located at $\eta_{\rm int}$ (blue line), while the bottom one is marked by the horizontal lines for each case.

interfacial region where the top solid cubes are located. This finding rules out the presence of shock waves and choking.

Figure 7 shows that the Darcy term and Forchheimer term in the momentum equation (19a) reach a comparable magnitude for all values of Ma, κ_p, and θ_{fp}. The Forchheimer correction is considerably lower than the Darcy drag for low κ_p (low d^*_{g0}) and θ_{fp}, but it increases and becomes slightly larger as either κ_p or θ_{fp} increase. This behavior is reported for all Mach numbers as shown in the right plot of Fig. 7, in which the free-stream conditions are fixed and the grain size and the porosity are gradually increased. Because the coefficient C_F is assumed to be a function of d^*_{g0} instead of d^*_g, this result suggests that the local similarity assumption holds better at moderate θ_{fp} and κ_p [24] for all Mach numbers.

The dimensional profiles of the streamwise velocity u^* and the static temperature T^* are computed at a distance $x^* = L^*$ from the leading edge and are plotted in Fig. 8 for the Mach-3 cases B1 and B2 and the Mach-6 cases C1 and C2. The physical coordinate y^* is computed by $y^* = x^*(2/\mathrm{Re}_x)^{1/2} \int_0^\eta T(\check{\eta})\mathrm{d}\check{\eta}$, where Re_x is the Reynolds number based on x^* [25]. The boundary-layer thickness of the Blasius solution (blue curve) compares well with the measurements of [52]

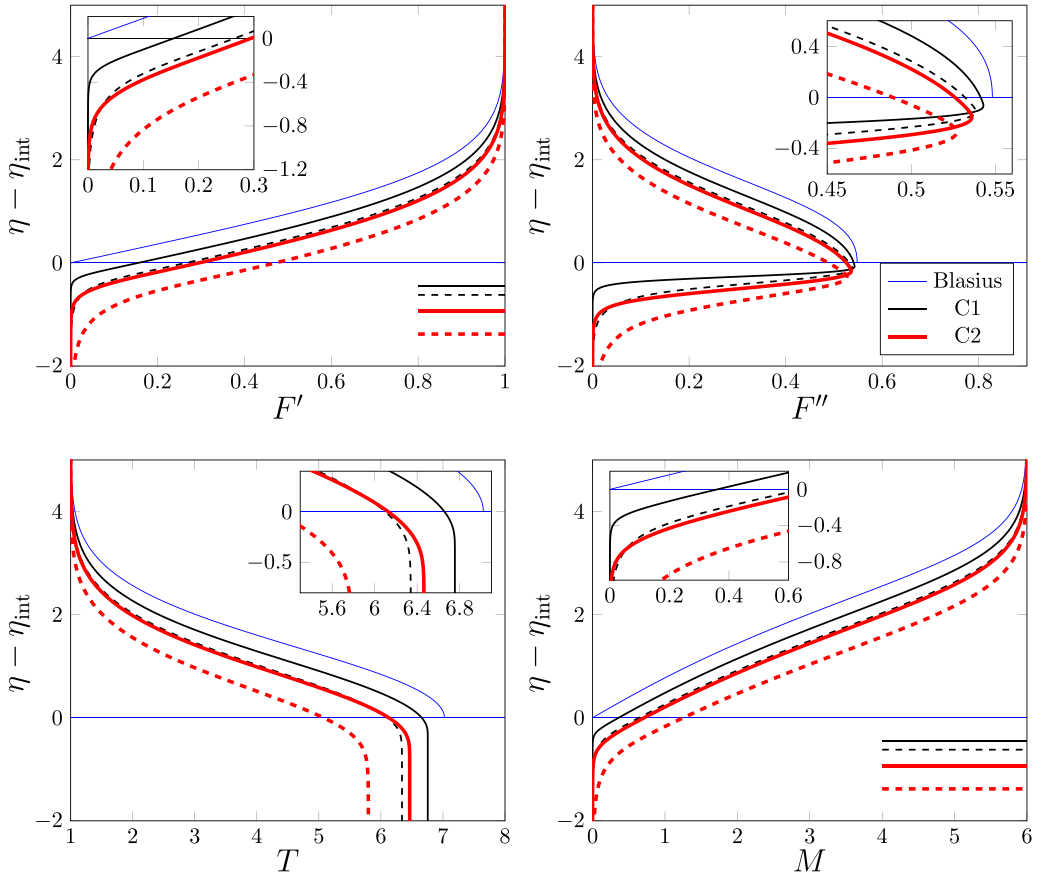

FIG. 6. First (top left) and second derivative (top right) of F as a function of η for a supersonic flow at $\text{Ma} = 6$. The static temperature T and the local Mach number M are shown in the bottom-left and bottom-right plots, respectively. The black and red curves show cases C1 and C2, respectively, for $\theta_{fp} = 0.85$ (solid) and $\theta_{fp} = 0.95$ (dashed). The Blasius solution over a nonpermeable wall is plotted in blue for comparison. The top boundary of the interfacial region is located at η_{int} (blue line), while the bottom one is marked by the horizontal lines for each case.

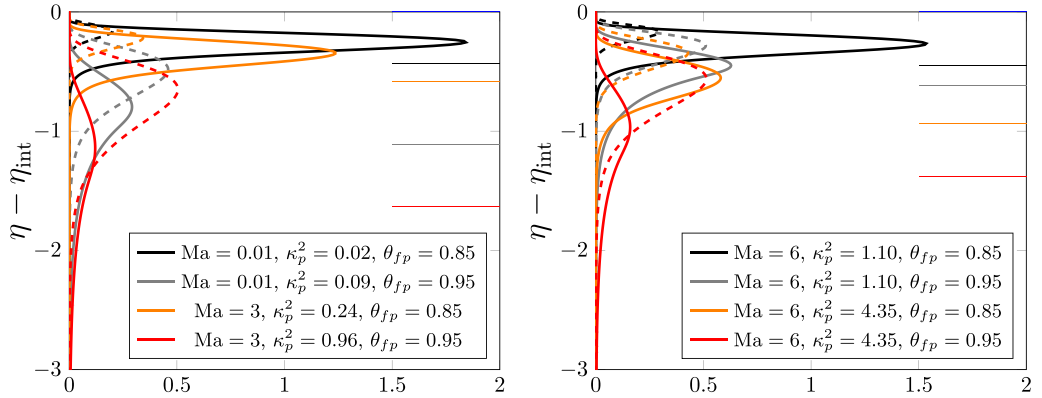

FIG. 7. Wall-normal profiles of the Darcy term (solid curves) and Forchheimer term (dashed curves) within the interfacial region. Left plot: cases A1, A2, B1, and B2. Right plot: C1 and C2.

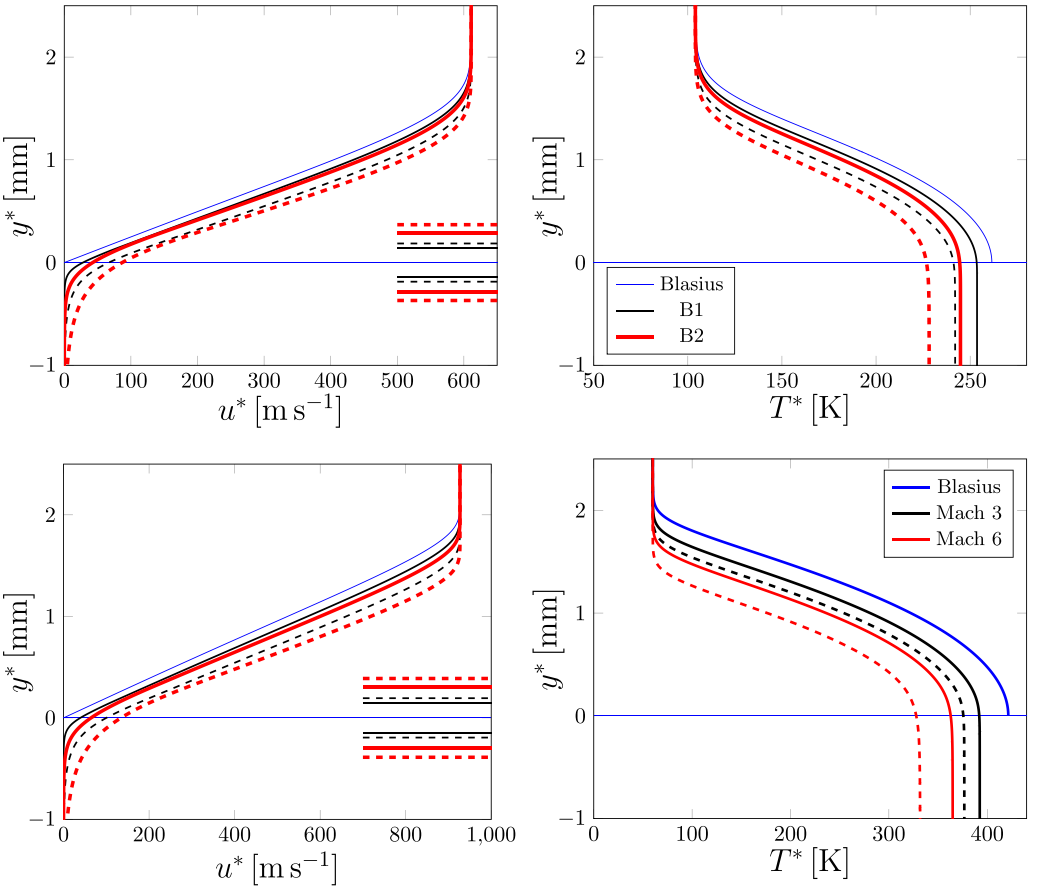

FIG. 8. Dimensional velocity and temperature profiles at a free-stream Mach number 3 (cases C1 and C2, top) and 6 (cases C1 and C2, bottom). The interfacial thickness is $\delta^*_{int} = 408\,\mu$m (B1 and C1, $\theta_{fp} = 0.85$), 525 µm (B1 and C1, $\theta_{fp} = 0.95$), 815 µm (B2 and C2, $\theta_{fp} = 0.85$), and 1051 µm (B2 and C2, $\theta_{fp} = 0.95$). The effect of varying θ_{fp} and d^*_{g0} is shown. The Mach-3 and Mach-6 adiabatic Blasius solution is plotted in blue.

and [53] (refer to Table I). When the substrate is sufficiently thick, the velocity profile decays quasiexponentially because only the diffusion and linear Darcy terms remain dominant underneath the interface, and the momentum equation (19a) reduces to the Darcy-Brinkman equation

$$\left(\frac{\mu}{T}F''\right)' - C_D\mu T\frac{(1-\theta_f)^2}{\theta_f^2}F' = 0. \tag{23}$$

This behavior is shown in Fig. 7: the Darcy terms (solid curves) decay more readily than the Forchheimer terms (dashed curves) underneath the interface. Hence, if the substrate is sufficiently thick, both F' and F'' are small at the bottom solid wall ($F'' \cong 10^{-4}$), which makes the choice of η_{int} arbitrary. Because the depth of the porous substrate is kept constant at $\eta_{\text{int}} = 10$ in the η-space and varies slightly in the y-space, the physical plots in Fig. 8 are offset and centered at the interface. Again, the velocity profiles shift towards the interface, and the boundary-layer thickness is reduced as both d^*_{g0} and θ_{fp} increase, while the temperature at the interface decreases. To better compare the porous-plate and the solid-plate results, the center of the interfacial region and the wall of the nonporous solution are placed at the same height in Fig. 8. The upper and lower boundaries of the

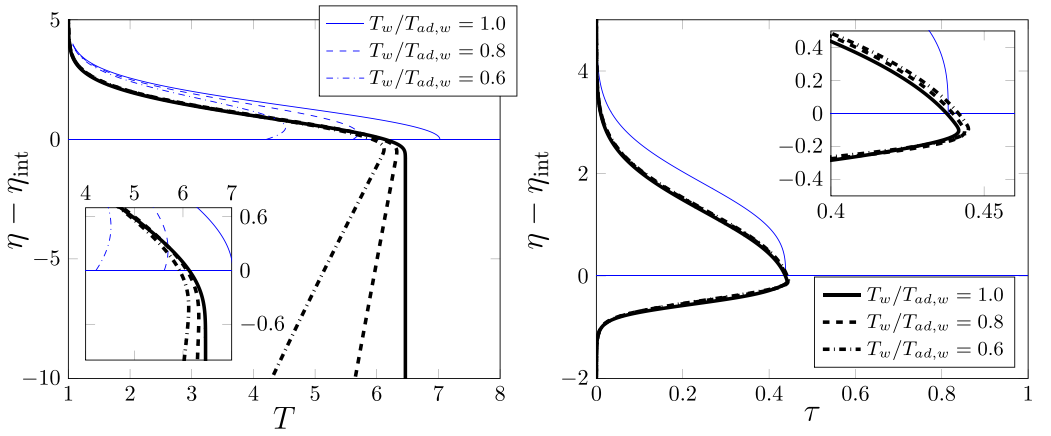

FIG. 9. Effect of the temperature boundary conditions at the bottom solid wall on the temperature profiles (left plot) and the shear stresses (right plot) at Ma $= 6$. The curves are computed for different values of $T_w/T_{\mathrm{ad},w}$, where $T_{\mathrm{ad},w} = 7.02$ is the adiabatic wall temperature of the Blasius solution. The blue curves represent the Blasius solution, and the black ones are the porous substrate solution (C2, $\theta_{fp} = 0.85$). The adiabatic recovery temperature at the solid wall is $T_{\mathrm{ad},w} = 6.46$.

interface are denoted here by the horizontal black and red lines. The departure of the velocity profile from the compressible Blasius solution is very small in the case C1, $\theta_{fp} = 0.85$. Only for larger porosities and grain sizes does the seepage become significant. This finding agrees qualitatively with the recent experiments of [20], who studied the development of a boundary layer over a porous substrate. Their measurements agreed well with the numerical results obtained from the computation of a no-slip, flat-plate, boundary-layer flow. They used a silicon-carbide foam porous insert with $\theta_{fp} = 0.862$ and 3.9 pores per linear millimeter, which corresponds to $d^*_{g0} = 130\,\mu\mathrm{m}$ in the present model. The present results suggest that porous media with higher θ_{fp} and d^*_{g0} should be used to affect the base flow significantly.

The effect of varying the temperature of the bottom solid wall is shown in Fig. 9 for the case C2, $\theta_{fp} = 0.85$. Because natural convection within the medium is not captured by the present model, wall-cooling conditions for which the bottom-wall temperature T_w is lower than the adiabatic recovery temperature of the substrate are considered. The temperature curves (Fig. 9, left plot) approach the adiabatic case as the ratio $T_w/T_{\mathrm{ad},w}$ increases. The temperature at the interface decreases from $T_w/T_{\mathrm{ad},w} = 1$ to $T_w/T_{\mathrm{ad},w} = 0.85$ with respect to the Blasius solution. However, as the ratio decreases further, the temperature at the interface remains higher and decreases linearly where the flow is stagnant. Equations (11c) and (19b) then reduce to the steady homogeneous heat conduction equation as in the model of [3]. Unlike in the Blasius boundary layer, where the temperature boundary condition at the solid wall directly affects the value of F'', the temperature condition imposed at the bottom of the porous substrate has no influence on F'' at the interface with the fluid region. The F' and F'' profiles are unaffected by the ratio $T_w/T_{\mathrm{ad},w}$ (refer to the right plot of Fig. 9). The results in Fig. 9 stem from the assumption of local thermal equilibrium of the fluid and solid phases, which may not be valid if the temperature at the bottom solid wall T_w departs the adiabatic condition $T_{w,\mathrm{ad}}$ significantly. The distribution of the compressible intrinsic shear stresses $\tau = \mu(F'' - F'\theta_f'/\theta_f)/(\theta_f T)$, shown in the plots in Fig. 10, is mostly affected by the geometry of the substrate, whereas the effect of $T_w/T_{\mathrm{ad},w}$ is again negligible. The peaks increase slightly and appear to be always located near the top boundary of the interface. A sharp reduction in the intrinsic shear stresses occurs in the free-fluid region above the interface when a substrate of high porosity is introduced.

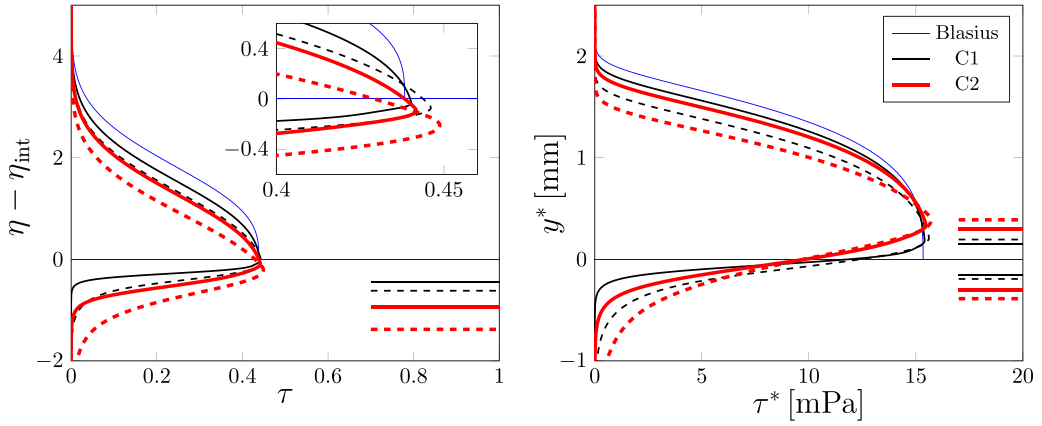

FIG. 10. Distribution of the intrinsic shear stresses for variable geometry (κ_p and θ_{fp}) in transformed (left) and real, dimensional coordinates at $x^* = L^*$ (right).

IV. SUMMARY

For the first time, a self-similar compressible laminar boundary layer flowing over an isotropic porous substrate of streamwise-increasing permeability is studied by asymptotic and numerical methods. This setup was considered in [5] for the incompressible case. Porous substrates with variable permeability may soon be manufactured, and their mathematical description allows for a self-similar solution of the boundary-layer equations. The solution includes a linear Darcy term and a quadratic Forchheimer correction. The volume averaged momentum and enthalpy balance equations become parabolic in the limit of high Reynolds and small Darcy numbers. The effect of the porous substrate is distilled in the distributions of the volume and surface porosity, the control parameter κ_p, and the Forchheimer coefficient C_F. The thicknesses of the interface and the boundary layer are comparable, and the volume and surface porosity vary smoothly therein. The wall-normal profiles of the streamwise velocity F', its wall-normal derivative F'', and the temperature T have been computed for different values of the Mach number, the control parameter, and the volume porosity below the interface. The profiles bear a strong resemblance to the Blasius solution for low values of κ_p and $\theta_{fp} \leqslant 0.85$. The slip velocity at the porous-free fluid interface increases and the shear stresses decrease sharply, as the volume porosity approaches unity. Wall cooling at the bottom solid boundary affects neither the velocity profiles nor the shear stresses when the porous substrate is sufficiently thick. A sharp reduction in the shear stresses and the static temperature is observed above the interface. This result shows that the introduction of a porous substrate of high porosity and permeability can substantially alter the properties of a supersonic laminar boundary layer, which is significant to flow control applications [19,20].

ACKNOWLEDGMENTS

The authors acknowledge support from the U.S. Air Force through the AFOSR Grant No. FA8655-21-1-7008. P.R. acknowledges support from EPSRC (Grant No. EP/T01167X/1). L.F. acknowledges support from the University of Sheffield Publication Scholarship.

L.F. wrote and proofread this manuscript, and developed, implemented, and visualized the presented material. P.R. conceptualized and supervised this work and contributed to the writing of the manuscript.

The authors have no relevant financial or nonfinancial interests to disclose.

DATA AVAILABILITY

The data that support the findings of this article are not publicly available upon publication because it is not technically feasible and/or the cost of preparing, depositing, and hosting the data would be prohibitive within the terms of this research project. The data are available from the authors upon reasonable request.

APPENDIX A: THE FORCHHEIMER TERM IN THE MOMENTUM EQUATION

The self-similar momentum equation (19a) is derived from the dimensional streamwise momentum balance equation (5), where only the leading-order terms are retained and the volume-averaging operators are omitted,

$$\theta_f\rho^*U^*\frac{\partial U^*}{\partial x^*}+\theta_f\rho^*V^*\frac{\partial U^*}{\partial y^*}=\frac{\partial}{\partial y^*}\left[\mu^*\frac{\partial(\theta_fU^*)}{\partial y^*}\right]-\theta_f^2\frac{\mu^*U^*}{K^*}-\theta_f^2\frac{c_F^*}{K^*}\rho^*U^{*2}+O(\mathrm{Re}^{-1}), \tag{A1}$$

and the form of $K^*(d_g^*)$ and $c_F^*(d_g^*=d_{g0}^*)$ that allows for a self-similar solution is used,

$$K^*(d_g^*)=\frac{\theta_f^3}{(1-\theta_f)^2}\frac{d_g^{*2}}{A}, \tag{A2a}$$

$$c_F^*(d_{g0}^*)=\frac{\theta_f}{1-\theta_f}\frac{d_{g0}^*}{B}. \tag{A2b}$$

The terms in (A1) are scaled by the reference quantities

$$\begin{aligned}&\frac{\rho_\infty^*U_\infty^*}{L^*}\left(\theta_f\rho U\frac{\partial U}{\partial x}+\theta_f\rho V\frac{\partial U}{\partial y}\right)\\&\quad=\frac{\mu_\infty^*U_\infty^*}{L^{*2}}\frac{\partial}{\partial y}\left[\mu\frac{\partial(\theta_fU)}{\partial y}\right]-\frac{\mu_\infty^*U_\infty^*}{d_{g0}^{*2}}\left(\frac{d_{g0}^*}{d_g^*}\right)^2\theta_f^2\frac{A(1-\theta_f)^2}{\theta_f^3}\mu U\\&\quad\quad-\frac{\rho_\infty^*U_\infty^{*2}}{d_{g0}^{*2}}\left(\frac{d_{g0}^*}{d_g^*}\right)^2\theta_f^2\frac{A(1-\theta_f)^2}{\theta_f^3}\frac{\theta_f}{1-\theta_f}\frac{d_{g0}^*}{B}\rho U^2,\end{aligned} \tag{A3}$$

and rearranged to obtain the leading-order balance for $A=O(1)$ and $B=O(\mathrm{Da}^{-1/2})$,

$$\begin{aligned}&\theta_f\rho U\frac{\partial U}{\partial x}+\theta_f\rho V\frac{\partial U}{\partial y}\\&\quad=\frac{\partial}{\partial y}\left[\mu\frac{\partial(\theta_fu)}{\partial y}\right]-\frac{\theta_f^2}{\mathrm{ReDa}}\left(\frac{d_{g0}^*}{d_g^*}\right)^2\left[A\frac{(1-\theta_f)^2}{\theta_f^3}\mu U+A\mathrm{ReDa}\frac{1-\theta_f}{\theta_f^2}\frac{\rho U^2}{B\mathrm{Da}^{1/2}}\right].\end{aligned} \tag{A4}$$

By introducing the identities $\rho T=1$, $C_D=A/\kappa_p^2=A(\mathrm{ReDa})^{-1}$, and $C_F=A/(B\mathrm{Da}^{1/2})$, and the velocity components (21), the momentum balance becomes

$$\begin{aligned}&(\alpha x)^{a+b-1}\alpha\frac{(b-a)}{\theta_f}\left(\frac{\partial F}{\partial\eta}\right)^2+(\alpha x)^{a+b}\frac{\partial F}{\partial\eta}\frac{\partial}{\partial x}\left(\frac{1}{\theta_f}\frac{\partial F}{\partial\eta}\right)_\eta\\&\quad-(\alpha x)^{a+b}\frac{\partial F}{\partial x}\bigg|_\eta\frac{\partial}{\partial\eta}\left(\frac{1}{\theta_f}\frac{\partial F}{\partial\eta}\right)-(\alpha x)^{a+b-1}\alpha bF\frac{\partial}{\partial\eta}\left(\frac{1}{\theta_f}\frac{\partial F}{\partial\eta}\right)\\&\quad=\frac{\partial}{\partial\eta}\left(\frac{\mu}{T}\frac{\partial^2F}{\partial\eta^2}\right)-(\alpha x)^{3b-a}\left(\frac{d_{g0}^*}{d_g^*}\right)^2\left[C_D\frac{(1-\theta_f)^2}{\theta_f^2}\mu T\frac{\partial F}{\partial\eta}+C_F\frac{1-\theta_f}{\theta_f^2}\left(\frac{\partial F}{\partial\eta}\right)^2\right],\end{aligned} \tag{A5}$$

where the symbol $\partial/\partial x|_\eta$ denotes the derivative with respect to x at constant η. The self-similar solution (19a) is recovered if $a = b = 1/2$, $\alpha = 2$, and $d_g^*/d_{g0}^* = (2x)^{1/2}$ [23].

APPENDIX B: NUMERICAL PROCEDURES

The governing equations are solved using the block-elimination method described in [54,55] and [22]. The ordinary differential equations (ODEs) (19) are decomposed into a system of first-order ODEs,

$$\theta_f^2(bv)' - \zeta_f f u + \theta_f f v - \left(1 - 2\theta_f + \theta_f^2\right) o u - (1-\theta_f) q u^2 = 0, \tag{B1a}$$

$$\theta_f(\theta_{\partial ff} e p)' + \theta_f f p + d v^2 = 0, \tag{B1b}$$

with the auxiliary equations $u = f'$, $v = u'$, and $p = g'$. Here,

$$f = F, \quad u = F', \quad v = F'', \quad g = T, \quad p = T', \tag{B2a}$$

$$b = \frac{\mu}{g}, \quad e = \frac{1}{\mathrm{Pr}}\frac{\mu}{g}, \quad d(\gamma-1)\mathrm{Ma}^2\frac{\mu}{g}, \quad o = C_D b g^2, \quad q = C_F, \tag{B2b}$$

and $\zeta_f = \theta_f'$. The nonlinearity of the first-order system (B1) is treated by Taylor-expanding the variables (B2a) in the residuals

$$\delta f = f - f^{(0)}, \quad \delta u = u - u^{(0)}, \quad \delta v = v - v^{(0)}, \quad \delta g = g - g^{(0)}, \quad \delta p = p - p^{(0)}, \tag{B3}$$

into the equations. The momentum and enthalpy balances (B1) and the auxiliary equations reduce to linearized equations for the residuals. The domain is discretized using uniform second-order finite differences centered in the midpoint $j - 1/2$, where $0 \leqslant j \leqslant N$, and N is the number of grid points along η,

$$\delta f_j - \delta f_{j-1} - \frac{h}{2}(\delta u_j + \delta u_{j-1}) = f_{j-1}^{(0)} - f_j^{(0)} + \frac{h}{2}\left(u_j^{(0)} + u_{j-1}^{(0)}\right) \equiv \left(r_1^{(0)}\right)_j, \tag{B4a}$$

$$(s_1)_j \delta v_j + (s_2)_j \delta v_{j-1} + (s_3)_j \delta f_j + (s_4)_j \delta f_{j-1} + (s_5)_j \delta u_j + (s_6)_j \delta u_{j-1} = \left(r_2^{(0)}\right)_j, \tag{B4b}$$

$$\begin{aligned}(\beta_1)_j \delta p_j + (\beta_2)_j \delta p_{j-1} + (\beta_3)_j \delta f_j + (\beta_4)_j \delta f_{j-1} + (\beta_5)_j \delta u_j \\ + (\beta_6)_j \delta u_{j-1} + (\beta_7)_j \delta g_j + (\beta_8)_j \delta g_{j-1} + (\beta_9)_j \delta v_j + (\beta_{10})_j \delta v_{j-1} = \left(r_3^{(0)}\right)_j,\end{aligned} \tag{B4c}$$

$$\delta u_{j+1} - \delta u_j - \frac{h}{2}(\delta u_{j+1} + \delta u_j) = u_j^{(0)} - u_{j+1}^{(0)} + \frac{h}{2}\left(u_{j+1}^{(0)} + u_j^{(0)}\right) \equiv \left(r_4^{(0)}\right)_j, \tag{B4d}$$

$$\delta g_{j+1} - \delta g_j - \frac{h}{2}(\delta p_{j+1} + \delta p_j) = g_j^{(0)} - g_{j+1}^{(0)} + \frac{h}{2}\left(p_{j+1}^{(0)} + p_j^{(0)}\right) \equiv \left(r_5^{(0)}\right)_j, \tag{B4e}$$

where $h = \eta_j - \eta_{j-1}$ is the grid size. The coefficients in (B4b) are

$$(s_1)_j = \left(\theta_f^2\right)_{j-1/2} h^{-1} b_j + (\theta_f)_{j-1/2} \frac{f_j^{(0)}}{2}, \tag{B5a}$$

$$(s_2)_j = -\left(\theta_f^2\right)_{j-1/2} h^{-1} b_{j-1} + (\theta_f)_{j-1/2} \frac{f_{j-1}^{(0)}}{2}, \tag{B5b}$$

$$(s_3)_j = -(\zeta_f)_{j-1/2} \frac{u_j^{(0)}}{2} + (\theta_f)_{j-1/2} \frac{v_j^{(0)}}{2}, \tag{B5c}$$

$$(s_4)_j = -(\zeta_f)_{j-1/2} \frac{u_{j-1}^{(0)}}{2} + (\theta_f)_{j-1/2} \frac{v_{j-1}^{(0)}}{2}, \tag{B5d}$$

$$(s_5)_j = -(\zeta_f)_{j-1/2} \frac{f_j^{(0)}}{2} - \left[1 - 2(\theta_f)_{j-1/2} + \left(\theta_f^2\right)_{j-1/2}\right] \frac{o_j}{2} - [1 - (\theta_f)_{j-1/2}](q u^{(0)})_j, \tag{B5e}$$

$$(s_6)_j = -(\zeta_f)_{j-1/2}\frac{f^{(0)}_{j-1}}{2} - \left[1 - 2(\theta_f)_{j-1/2} + \left(\theta_f^2\right)_{j-1/2}\right]\frac{o_{j-1}}{2} - [1 - (\theta_f)_{j-1/2}](qu^{(0)})_{j-1}, \tag{B5f}$$

$$\begin{aligned}(r_2)_j = &-\left(\theta_f^2\right)_{j-1/2}h^{-1}[(bv^{(0)})_j - (bv^{(0)})_{j-1}] + (\zeta_f)_{j-1/2}(f^{(0)}u^{(0)})_{j-1/2} \\ &- (\theta_f)_{j-1/2}(f^{(0)}v^{(0)})_{j-1/2} + \left[1 - 2(\theta_f)_{j-1/2} + \left(\theta_f^2\right)_{j-1/2}\right](ou^{(0)})_{j-1/2} \\ = &+ [1 - (\theta_f)_{j-1/2}](qu^{(0)2})_{j-1/2},\end{aligned} \tag{B5g}$$

and the coefficients in (B4c) are

$$(\beta_1)_j = (\theta_f)_{j-1/2}\left[h^{-1}(\theta_{\partial ff}e)_j + \frac{f^{(0)}_j}{2}\right], \tag{B6a}$$

$$(\beta_2)_j = (\theta_f)_{j-1/2}\left[-h^{-1}(\theta_{\partial ff}e)_{j-1} + \frac{f^{(0)}_{j-1}}{2}\right], \tag{B6b}$$

$$(\beta_3)_j = (\theta_f)_{j-1/2}\frac{p^{(0)}_j}{2}, \tag{B6c}$$

$$(\beta_4)_j = (\theta_f)_{j-1/2}\frac{p^{(0)}_{j-1}}{2}, \tag{B6d}$$

$$(\beta_5)_j = (\beta_6)_j = (\beta_7)_j = (\beta_8)_j = 0, \tag{B6e}$$

$$(\beta_9)_j = (dv^{(0)})_j, \tag{B6f}$$

$$(\beta_{10})_j = (dv^{(0)})_{j-1}, \tag{B6g}$$

$$\begin{aligned}(r_3)_j = &-(\theta_f)_{j-1/2}h^{-1}[(\theta_{\partial ff}ep^{(0)})_j - (\theta_{\partial ff}ep^{(0)})_{j-1}] \\ &- (\theta_f)_{j-1/2}(f^{(0)}p^{(0)})_{j-1/2} - (dv^{(0)2})_{j-1/2}.\end{aligned} \tag{B6h}$$

The system (B4) is elliptic in η. Three boundary conditions $\delta f_0 = \delta u_0 = \delta p_0 = 0$ are imposed at the bottom solid wall $j = 0$, and two boundary conditions $\delta u_{N-1} = \delta g_{N-1} = 0$ are imposed in the free stream $j = N - 1$. Following [22], the system (B4) is written in the matrix form

$$\underline{\underline{\boldsymbol{B}}}_j\underline{\boldsymbol{\delta}}_{j-1} + \underline{\underline{\boldsymbol{A}}}_j\underline{\boldsymbol{\delta}}_j + \underline{\underline{\boldsymbol{C}}}_j\underline{\boldsymbol{\delta}}_{j+1} = \underline{\boldsymbol{r}}^{(\mathbf{0})}{}_j, \tag{B7}$$

where $\underline{\boldsymbol{\delta}} = [\delta f \quad \delta u \quad \delta v \quad \delta g \quad \delta p]^T$ is the vector of the residuals, $\underline{\boldsymbol{r}}^{(\mathbf{0})} = [r_1^{(0)} \quad r_2^{(0)} \quad r_3^{(0)} \quad r_4^{(0)} \quad r_5^{(0)}]^T$ is the vector of the equations for the variables $f^{(0)}$, $u^{(0)}$, $v^{(0)}$, $g^{(0)}$ and $p^{(0)}$, and $\underline{\underline{\boldsymbol{B}}}_j$, $\underline{\underline{\boldsymbol{A}}}_j$ and $\underline{\underline{\boldsymbol{C}}}_j$ are the coefficient matrices. A tridiagonal block-elimination (Thomas) algorithm is employed to compute the vector of the residuals $\underline{\boldsymbol{\delta}}$ in (B7). The residuals are then used to update $f^{(0)}$, $u^{(0)}$, $v^{(0)}$, $g^{(0)}$, and $p^{(0)}$ through (B3), and the whole procedure is repeated iteratively until the magnitude of $|\underline{\boldsymbol{\delta}}|$ falls below the prescribed tolerance 10^{-12}.

[1] D. A. Nield and A. Bejan, *Convection in Porous Media* (Springer International, New York, 2017).

[2] K. Vafai and S.-J. Kim, Analysis of surface enhancement by a porous substrate, J. Heat Transf. **112**, 700 (1990).

[3] D. A. Nield and A. V. Kuznetsov, Boundary-layer analysis of forced convection with a plate and porous substrate, Acta Mech. **166**, 141 (2003).

[4] W. P. Breugem, B. J. Boersma, and R. E. Uittenbogaard, The laminar boundary layer over a permeable wall, Transp. Porous Media **59**, 267 (2005).
[5] K. Tsiberkin On the structure of the steady-state flow velocity field near the interface between a homogeneous liquid and a Brinkman porous medium, Tech. Phys. **61**, 1181 (2016).
[6] W. P. Breugem, B. J. Boersma, and R. E. Uittenbogaard, The influence of wall permeability on turbulent channel flow, J. Fluid Mech. **562**, 35 (2006).
[7] Z. Wu and P. Mirbod, Experimental analysis of the flow near the boundary of random porous media, Phys. Fluids **30**, 047103 (2018).
[8] J. Härter, D. S. Martínez, R. Poser, B. Weigand, and G. Lamanna, Coupling between a turbulent outer flow and an adjacent porous medium: high resolved particle image velocimetry measurements, Phys. Fluids **35**, 022105 (2023).
[9] M. Kaviany, Boundary-layer treatment of forced convection heat transfer from a semi-infinite flat plate embedded in porous media, J. Heat Transf. **109**, 345 (1987).
[10] A. Nakayama, T. Kokudai, and H. Koyama, Non-Darcian boundary layer flow and forced convective heat transfer over a flat plate in a fluid-saturated porous medium, J. Heat Transf. **112**, 157 (1990).
[11] M. V. Papalexandris, Boundary-layer flow in a porous domain above a flat plate, J. Eng. Math. **140**, 4 (2023).
[12] G. Neale and W. Nader, Practical significance of Brinkman's extension of Darcy's law: coupled parallel flows within a channel and a bounding porous medium, Can. J. Chem. Eng. **52**, 475 (1974).
[13] J. A. Ochoa-Tapia and S. Whitaker, Momentum transfer at the boundary between a porous medium and a homogeneous fluid–I. Theoretical development, Int. J. Heat Mass Transf. **38**, 2635 (1995).
[14] D. A. Nield, Modelling high speed flow of a compressible fluid in a saturated porous medium, Transp. Porous Media **14**, 85 (1994).
[15] J. Bear and Y. Bachmat, *Introduction to Modeling of Transport Phenomena in Porous Media* (Kluwer Academic, Dordrecht, 1990).
[16] S. Whitaker, *The Method of Volume Averaging* (Kluwer Academic, Dordrecht, 1998).
[17] A De Ville, On the properties of compressible gas flow in a porous media, Transp. Porous Media **22**, 287 (1996).
[18] S. G. Mironov, A. A. Maslov, T. V. Poplavskaya, and S. V. Kirilovskiy, Modeling of a supersonic flow around a cylinder with a gas-permeable porous insert, J. Appl. Mech. Tech. Phys. **56**, 549 (2015).
[19] A. A. Maslov, S. G. Mironov, T. V. Poplavskaya, and S. V. Kirilovskiy, Supersonic flow around a cylinder with a permeable high-porosity insert: experiment and numerical simulation, J. Fluid Mech. **867**, 611 (2019).
[20] C. L. Running, B. L. Bemis, J. L. Hill, M. P. Borg, J. J. Redmond, K. Jantze, and C. Scalo, Attenuation of hypersonic second-mode boundary-layer instability with an ultrasonically absorptive silicon-carbide foam, Exp. Fluids **64**, 79 (2023).
[21] E. M. Sparrow, H. Quack, and C. J. Boerner, Local nonsimilarity boundary-layer solutions, AIAA J. **8**, 1936 (1970).
[22] T. Cebeci, *Convective Heat Transfer* (Horizons, Heidelberg, 2002).
[23] K. Tsiberkin, Effect of inertial terms on fluid-porous medium flow coupling, Transp. Porous Media **121**, 109 (2018).
[24] K. Tsiberkin, Inertial and Darcy's terms ratio in boundary layer at fluid-porous medium interface, Transp. Porous Media **125**, 259 (2018).
[25] K. Stewartson, *The Theory of Laminar Boundary Layers in Compressible Fluids* (Clarendon Press, Oxford, 1964).
[26] J. D. Anderson, *Hypersonic and High-temperature Gas Dynamics* (AIAA, Reston, Virginia, USA, 2019).
[27] S. Whitaker, Advances in theory of fluid motion in porous media, Ind. Eng. Chem. **61**, 14 (1969).
[28] Y. Bachmat and J. Bear, Macroscopic modelling of transport phenomena in porous media. 1: the continuum approach, Transp. Porous Media **1**, 213 (1986).
[29] S. Sorek, D. Levi-Hevroni, A. Levy, and G. Ben-Dor, Extensions to the macroscopic Navier-Stokes equation, Transp. Porous Media **61**, 215 (2005).

[30] M. Quintard and S. Whitaker, Transport in ordered and disordered porous media II: generalized volume averaging, Transp. Porous Media **14**, 179 (1994).
[31] W. P. Breugem and B. J. Boersma, Direct numerical simulations of turbulent flow over a permeable wall using a direct and a continuum approach, Phys. Fluids **17**, 025103 (2005).
[32] W. G. Gray, A derivation of the equations for multi-phase transport, Chem. Eng. Sci. **30**, 229 (1975).
[33] S. Whitaker, Flow in porous media I: a theoretical derivation of Darcy's law, Transp. Porous Media **1**, 3 (1986).
[34] S. Whitaker, The Forchheimer equation: a theoretical development, Transp. Porous Media **25**, 27 (1996).
[35] D. Lasseux and F. J. Valdés-Parada, On the developments of Darcy's law to include inertial and slip effects, C. R. Méc. **345**, 660 (2017).
[36] Z. Khalifa, L. Pocher, and N. Tilton, Regimes of flow through cylinder arrays subject to steady pressure gradients, Int. J. Heat Mass Transf. **159**, 120072 (2020).
[37] J. Barrère, O. Gipouloux, and S. Whitaker, On the closure problem for Darcy's law, Transp. Porous Media **7**, 209 (1992).
[38] A. Costa, Permeability-porosity relationship: a reexamination of the kozeny-carman equation based on a fractal pore-space geometry assumption, Geophys. Res. Lett. **33**, L02318 (2006).
[39] M. D. M. Innocentini, P. Sepulveda, and F. S. Ortega, *Permeability* (Wiley-VCH, 2006), Chap. 4.2.
[40] H. Wedin and S. Cherubini, Permeability models affecting nonlinear stability in the asymptotic suction boundary layer: the Forchheimer versus the Darcy model, Fluid Dyn. Res. **48**, 061411, (2016).
[41] D. A. Nield, The limitations of the Brinkman-Forchheimer equation in modeling flow in a saturated porous medium and at an interface, Int. J. Heat Fluid Flow **12**, 269 (1991).
[42] N. Tilton and L. Cortelezzi, Stability of boundary layers over porous walls with suction, AIAA J. **53**, 2856 (2015).
[43] N. Tilton and L. Cortelezzi, Linear stability analysis of pressure-driven flows in channels with porous walls, J. Fluid Mech. **604**, 411 (2008).
[44] G. Emanuel and J. P. Jones, Compressible flow through a porous plate, Int. J. Heat Mass Transf. **11**, 827 (1968).
[45] R. P. Shreeve, Supersonic flow from a porous metal plate, AIAA J. **6**, 752 (1968).
[46] M. Celli, D. A. S. Rees, and A. Barletta, The effect of local thermal non-equilibrium on forced convection boundary layer flow from a heated surface in porous media, Int. J. Heat Mass Transf. **53**, 3533 (2010).
[47] M. V. Papalexandris, Thermal boundary-layer solutions for forced convection in a porous domain above a flat plate, J. Eng. Math. **144**, 3 (2024).
[48] M. van Dyke, *Perturbation Methods in Fluid Mechanics* (Parabolic, Stanford, 1975).
[49] P. S. Negi, M. Mishra, and M. Skote, DNS of a single low-speed streak subject to spanwise wall oscillations, Flow, Turbul. Combust. **94**, 795 (2015).
[50] A. Goharzadeh, A. Khalili, and B. B. Jørgensen, Transition layer thickness at a fluid-porous interface, Phys. Fluids **17**, 057102 (2005).
[51] W. P. Breugem, The influence of wall permeability on laminar and turbulent flows: theory and simulations, PhD. thesis, TU Delft, 2005.
[52] P. Graziosi and G. L. Brown, Experiments on stability and transition at Mach 3, J. Fluid Mech. **472**, 83 (2002).
[53] A. A. Maslov, A. N. Shiplyuk, A. A. Sidorenko, and D. Arnal, Leading-edge receptivity of a hypersonic boundary layer on a flat plate, J. Fluid Mech. **426**, 73 (2001).
[54] H. B. Keller and T. Cebeci, Accurate numerical methods for boundary layer flows i: two dimensional laminar flows, in *Proceedings of the Second International Conference on Numerical Methods in Fluid Dynamics*, edited by M. Holt (Springer, Berlin, 1971), pp. 92–100.
[55] H. B. Keller and T. Cebeci, Accurate numerical methods for boundary-layer flows II: two dimensional turbulent flows, AIAA J. **10**, 1193 (1972).